


Polarization optical switching between supercell states of plasmonic metasurfacesSeyed M. Sadeghi ^{1,*}, Dustin T. Roberts ¹, Rithvik R. Gutha¹, Steven Allen¹, and Christina Sharp²¹*Department of Physics and Astronomy, University of Alabama in Huntsville, Huntsville, Alabama 35899, USA*²*Department of Physics and Astronomy, University of Exeter, Exeter EX4 4QL, United Kingdom*

(Received 22 July 2022; accepted 9 December 2022; published 26 December 2022)

We study, experimentally and numerically, in-plane light scattering (side scattering) and near- and far-field collective excitations in plasmonic metasurfaces consisting of periodic arrays of Au V-shaped nanoantennas. Each unit cell in these arrays includes a pair of such nanoantennas facing each other ($<+>$). We show that, depending on the polarization of the incident light, such metasurfaces can support two types of supercells ($<+>$ and $>+<$). $<+>$ is a bracket supercell wherein two nanoantennas of the same unit cells are coupled to each other via their plasmonic fields. When the polarization of the incident light is rotated by 90° , a plasmonic conjugate supercell is formed ($>+<$). In this case the plasmon fields couple two V-shaped nanoantennas of the neighboring cells, supporting a geometrical and near-field coupling process different from $<+>$. We show that bracket and conjugate supercells support sharp infrared resonances at two different wavelengths, offering a high extinction polarization optical switching process associated with the transition between $<+>$ and $>+<$. Our results show that while $<+>$ supercells tend to be optically noninteracting with each other, $>+<$ supercells can get coupled to the lattice modes, spatially extending coherent properties across the arrays. We investigate the in-plane scattering of these arrays, demonstrating how variations of the charge configuration and phase by the incident light polarization can be used to coherently control the in-plane scattering of V-shaped nanoantennas arrays.

DOI: [10.1103/PhysRevA.106.063518](https://doi.org/10.1103/PhysRevA.106.063518)**I. INTRODUCTION**

Plasmonic metasurfaces are appealing hosts for investigation of many interesting phenomena with useful applications, ranging from optical devices to quantum photonics and quantum sensors [1–7,8]. The key feature of such materials is their capability to offer unique electromagnetic properties via variations of shapes and sizes of metallic nanostructures [9]. One type of metasurface that has gained some attention recently consists of V-shaped nanoantennas [10,11]. Such nanoantennas induce abrupt phase shifts in their optical paths, supporting two spatially separated charge oscillation modes [3]. It has been shown that such nanoantennas can be used for broadband anisotropic optical elements [8], quarter waveplates [2,7], negative refractive index [4], and aberration-free ultrathin flat lenses at telecom frequencies [1].

The prominent aspects of plasmonic metasurfaces can be further enhanced if their localized plasmonic modes are coherently coupled to optical lattice modes. Such a coupling process has been investigated extensively in arrays of metallic nanostructures and dielectrics, demonstrating formation of surface lattice resonances (SLRs) [12]. When SLRs happen, the plasmonic modes of individual nanoantennas are in phase with each other, expanding coherent information over the arrays. Surface lattice resonances are known to have applications ranging from biological and chemical sensing [13–20] to excitonic laser systems and multimodal nanolasers [21–23] and transfer of spin memory to the spontaneous emission of quantum emitters [24]. Recent reports have also shown

that SLRs can be supported by coherent excitations of localized surface plasmon resonances of templated nanoislands with random shapes and sizes, offering unique avenues for investigation of coherent networks of dipole domains and phase-correlated nanoantennas [25–27].

By means of experimental and numerical techniques, in this paper we study in-plane light scattering (side scattering) and far- and near-field coupling processes in plasmonic metasurfaces consisting of arrays of V-shaped nanoantennas. As shown in Fig. 1(a), the unit cells of these arrays consist of a pair of such nanoantennas facing each other ($<+>$). We show that these arrays can support the formation of polarization-dependent modes wherein two V-shaped nanoantennas are coupled to each other with different configurations via the plasmonic fields associated with the orthogonal modes of the nanoantennas. These polarization-switchable modes are associated with the cases wherein two V-shaped nanoantennas are coupled to each other either face to face, forming a bracket supercell ($<+>$), or back to back, generating a plasmonic conjugate supercell ($>+<$). We demonstrate that these cells offer near-unity extinctions at two different infrared wavelengths while offering two different categories of plasmonic coupling and hybridization. Our results also show that the $>+<$ supercell can support diffractive optical coupling wherein the supercells are coupled to the lattice modes, projecting the possibility of a SLR associated with coherent orthogonal coupling of such supercells. For the case of $<+>$, however, the results suggest nearly complete optical isolation, via lack of optical diffraction. These results suggest a polarization optical switching wherein rotation of the incident light polarization can lead to a transition between $>+<$ and $<+>$ supercell states.

*seyed.sadeghi@uah.edu

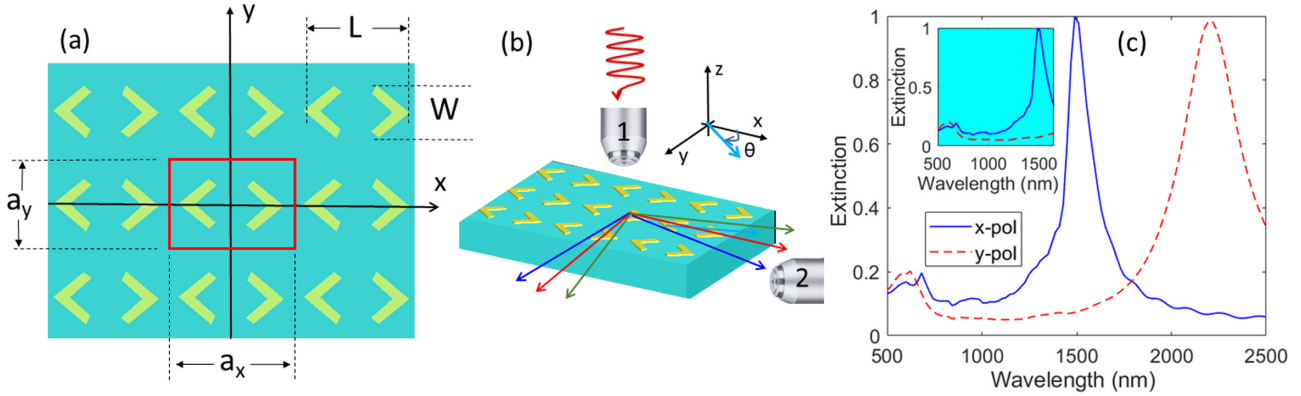


FIG. 1. (a) Schematic of arrays of Au V-shaped nanoantenna, (b) sketch of the experimental setup used to measure in-plane scattering along the x and y axes, and (c) simulation results for the extinction spectra of the $\langle \rangle$ arrays with the incident light polarization is along the x axis (solid line) and y axis (dashed line). The inset in (c) shows the spectra in the wavelength range compatible with the experimental results.

In this paper we also study the in-plane scattering of the arrays of the V-shaped nanoantennas when the incident light reaches the samples at normal angles [Fig. 1(b)]. This includes investigation of far-field scattering of the $\langle \rangle$ arrays at frequencies wherein the localized multipolar plasmon modes associated with such nanoantennas are prominently excited. We study in particular the in-plane scattering efficiency and polarization under different incident light polarization [Fig. 1(b)]. Our results suggest that this provides the possibility of controlling the charge configurations and localized plasmonic oscillations associated with the arms of the V-shaped nanoantennas. This in turn allows one to control the phase of the in-plane scattered light associated with each nanoantenna, offering a unique possibility to manipulate the spectra and polarization states of the in-plane scattered light by the incident light polarization. This is particularly distinct in the case when the incident polarization becomes parallel or perpendicular to the arms of the nanoantennas, allowing their longitudinal and transverse plasmon modes to become dominant.

Note that recent reports have shown unidirectional in-plane scattering of plane waves by individual V-shaped metal nanoantennas [28,29]. These reports also include V-shaped Si nanoantennas, showing broadband transverse light scattering [30]. V-shaped dielectric nanoantennas have also been used for bidirectional scattering and routing applications [31]. Additionally, recent reports have utilized in-plane scattering of arrays of nanoantennas to identify radiation associated with the Brillouin zone edges of metallic nanoantenna arrays [32], study scattering of gold nanoparticle trimers [33], and explore directional light scattering by single-element triangular plasmonic nanoparticles [34].

II. SUPERCELLS IN V-SHAPED NANOANTENNA ARRAYS

We start with the simulation results for the optical responses of the $\langle \rangle$ arrays, exploring the concepts of the supercells and their coherent optical coupling and switching. For this we used the finite-difference time domain provided by Device Multiphysics Simulation Suite of Lumerical software (2020a version). The structural design included, as shown in Fig. 1(a), a unit lattice cell consisting of two Au V-shaped nanoantennas ($\langle \rangle$) with length L , width W , and height H .

This unit had periodic boundary conditions along the x and y axes, while a planar white light was considered to reach the sample along the $-z$ axis. The periodic boundary conditions projected a two-dimensional arrays of $\langle \rangle$ with the lattice constants of a_x and a_y . To be consistent with the experimental results, simulations were carried out considering $L = 1000$ nm and $W = 430$ nm. The heights of the V-shaped nanoantennas were considered to be 40 nm, $a_x = 1.5$ μm , and $a_y = 1$ μm . The mesh sizes were considered to be 2 nm along the x and y axes and 4 nm along the z axis. The substrate was considered to be glass, selected from the library of the software. The superstrate had a refractive index of 1, i.e., referring to the case of air.

The results of the simulations for the extinction spectra of the array when the incident light was polarized along the x axis (x polarization) and y axis (y polarization) are shown in Fig. 1(c). These results show that for x polarization two peaks can be seen, one with small amplitude at about 680 nm and another one with a high amplitude at 1490 nm (solid line). For y polarization, however, the shorter-wavelength peak occurs at about 600 nm and the longer-wavelength peak at 2196 nm (dashed line). A unique feature of these results is that the infrared peaks, occurring at 1490 and 2196 nm, support high extinction values, close to unity. Additionally, the peak at 1490 nm is much narrower than that at 2196 nm. These results suggest a polarization optical switching process wherein a 90° rotation of the incident light polarization can lead to a distinct shift of the extinction peak in the infrared range.

The results for the mode field enhancement profiles, i.e., ratio of the squared fields in the presence and absence of the nanoantennas, in the x - y planes for x polarization are shown in Fig. 2. These planes were considered to be 20 nm above the glass substrate, i.e., passing through the middle of the heights of the nanoantennas. At 680 nm these results suggest concentration of the near fields at the corners and the sides of the V-shaped nanoantennas [Fig. 2(a)]. This mode can refer to quadrupole modes (Q_x) of the V-shaped nanoantennas for x polarization [28,29]. As depicted in Fig. 3(a), one expects that this mode supports accumulation of charges with opposite signs at the corner of the V-shaped nanoantennas in the adjacent unit cells. Figure 2 suggests that at longer wavelengths this field configuration changes dramatically. At 1490 nm,

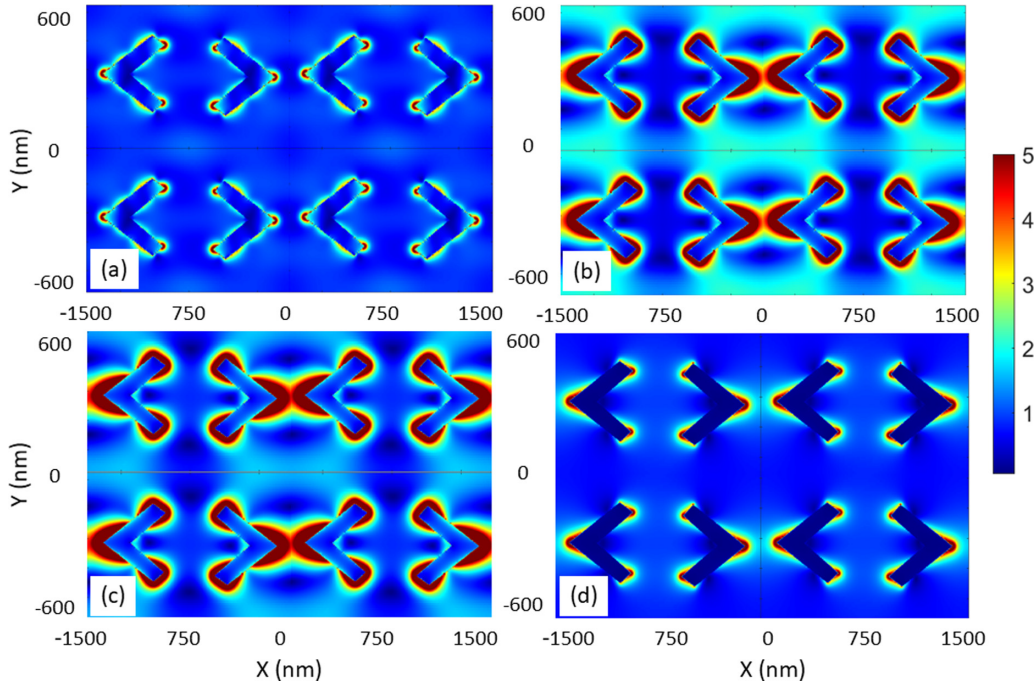


FIG. 2. Field enhancement mode profiles associated with the results shown in Fig. 1(c) for x polarization in the x - y plane at (a) 680, (b) 1490, (c) 1510, and (d) 2500 nm. The x - y plane here passes approximately through the middle of the height of the nanoantennas, i.e., 20 nm from the substrate. The scale bar refers to the amount of field enhancement, which is unitless.

i.e., the wavelength of the infrared peak associated with x polarization [Fig. 1(c), solid line], one can see a back-to-back coupling of pairs of nanoantennas, forming a plasmonic conjugate configuration, i.e., $> + <$ supercells [Fig. 2(b)]. This process can be associated with the coupling of dipoles of two V-shaped antennas (D_x) in two adjacent unit cells [Fig. 3(b)].

An interesting feature seen in the results shown in Fig. 2(b) is the evidence of optical coupling of these supercells along the y axis via diffraction. This suggests the possibility of

formation of a SLR associated with the orthogonal hybridization of the lattice modes with $> + <$ supercells. This can be understood considering the fact that since $a_y = 1 \mu\text{m}$ the Rayleigh wavelength, given by $\lambda_{\text{Ra}} = n[1 + \cos(\beta)]$, is equal to about $1.45 \mu\text{m}$. Here n is the substrate refractive index, considered to be 1.45, and $\beta = 0^\circ$ is the angle of the incident light. The intersubcell diffractive feature starts to disappear at longer wavelength [Fig. 2(c)]. At 2500 nm, only a weak residue of $> + <$ remains and the lattice mode disappears [Fig. 2(d)]. Note that the assumption of $n = 1.45$ requires that the optical modes mostly reside in the substrate, which will be shown in the following. Additionally, here the system under consideration is not homogeneous, i.e., the refractive indices of the substrate and superstrate are different. Although this presents more demanding conditions [35–37], with large enough plasmonic polarizability such a system can support strong enough Rayleigh coupling to form SLR [12,19,38,39].

Next we rotated the polarization by 90° so that it became aligned along the y axes of the array (y polarization). The results suggest the formation of different types of modes. As shown in Fig. 4(a), at about 600 nm these modes are associated with multipolar plasmonic modes associated with y polarization (Q_y). At 660 nm, these modes are enhanced, indicating the formation of unique quadrupolar features of the V-shaped nanoantennas [28]. Figure 3(c) shows the schematic of the charge configuration associated with this case. At 883 nm the charge concentrations at the corners of the V-shaped nanoantennas seem to be diminished to some extent, forming modes that are extended from one arm of a given nanoantenna to its other arm [Fig. 4(c)]. This indicates excitation of dipole modes associated with y polarization (D_y) [28]. As schematically shown in Fig. 3(d), under

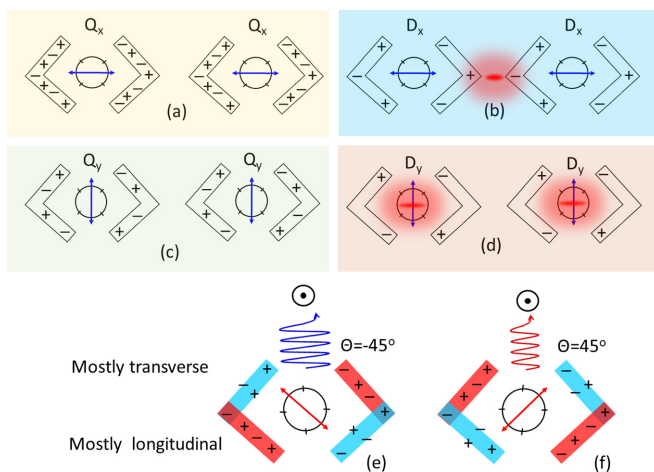


FIG. 3. Schematics of the charge configurations associated with (a) quadrupoles Q_x and (b) dipoles D_x of the V-shaped nanoantennas for x polarization and (c) quadrupoles Q_y and (d) dipoles D_y for y polarization. Also shown are the charge configurations for the cases when (e) $\theta = -45^\circ$ and (f) $\theta = 45^\circ$.

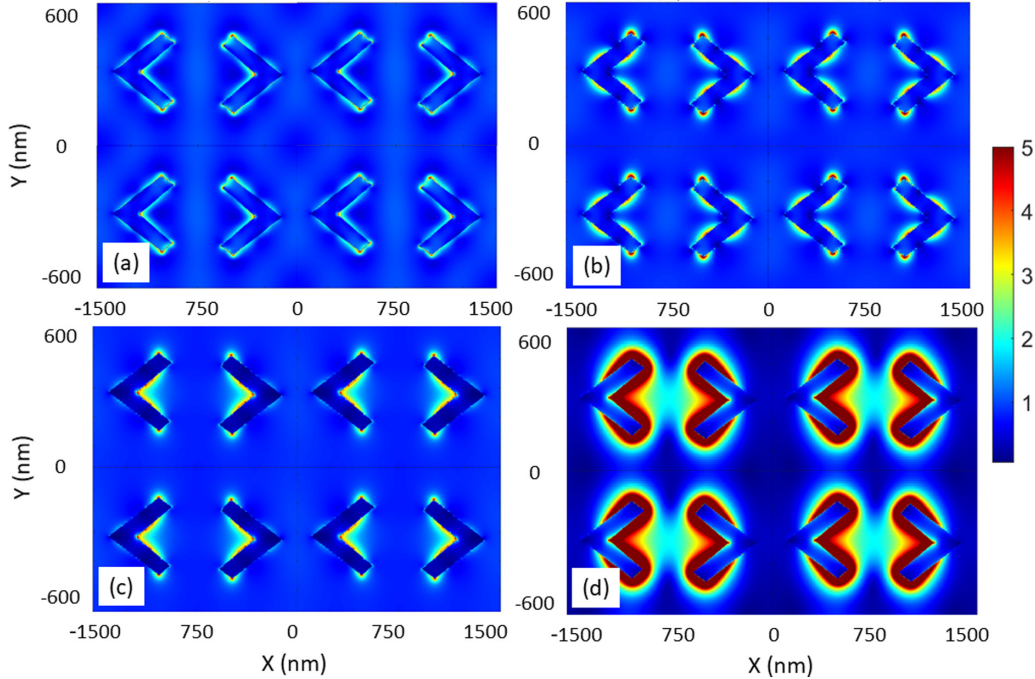


FIG. 4. Field enhancement mode profiles associated with the results shown in Fig. 1(c) for y polarization in the x - y plane at (a) 600, (b) 660, (c) 883, and (d) 2196 nm. The x - y plane here passes approximately through the middle of the height of the nanoantennas, i.e., 20 nm from the substrate. The scale bar refers to the amount of field enhancement, which is unitless.

this condition the charges at the corners of the V-shaped nanoantennas are diminished, while they are concentrated at the ends of their two arms. At 2196 nm this feature becomes more prominent as two antennas within a single unit cell are coupled to each other, forming a bracket supercell ($<+>$). The results in Fig. 4(d) suggest that these supercells are optically isolated from each other.

Figure 5 shows the modal field enhancement profiles in the x - z planes under the conditions that $>+<$ [Fig. 5(a)] and $<+>$ [Fig. 5(b)] supercells are formed. This plane is perpendicular to the substrate and includes the x axis [Fig. 1(a)].

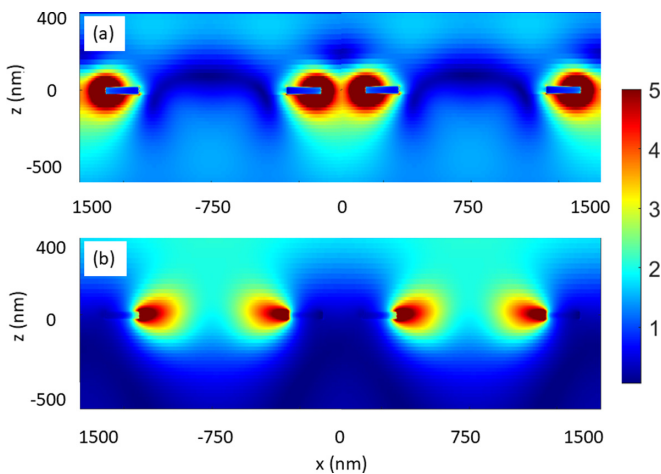


FIG. 5. Field enhancement mode profiles associated with the results for (a) x polarization at 1490 nm and (b) y polarization at 2196 nm in the x - z plane for (a) $>+<$ and (b) $<+>$ supercells. The scale bar refers to the amount of field enhancement.

In the case of $>+<$ supercell, the results suggest that the plasmonic-photonic modes are mostly localized in the substrate [Fig. 5(a)]. Therefore, the optical coupling of the plasmon modes associated with such supercells mostly occurs in the substrate. This also leads to less sensitivity to variations of the refractive index of the superstrate [Fig. 5(a)]. On the other hand, for the case of $<+>$ modes the plasmon mode is highly localized in the superstrate [Fig. 5(b)]. Therefore, this mode should show a relatively high sensitivity to the environment.

III. EXPERIMENTAL METHODS

To experimentally test the results presented in the preceding section we used electron-beam lithography to fabricate two types of samples. These samples contain arrays of Au $<>$ with average sizes of $L = 1000$ nm and $W = 430$ nm. The thickness of nanoantennas was about 40 nm. The lattice constants of sample 1 were $a_x = 1.5$ μm and $a_y = 1$ μm [Fig. 6(a), inset] and for sample 2 $a_x = 3$ μm and $a_y = 2$ μm [Fig. 6(b), inset]. Figure 6(a) shows the optical image of sample 1, indicating a uniform fabrication process and overall structural features of the sample. To measure the extinction spectra of these arrays, we used a broadband halogen lamp in a transmission optical setup. In this setup the incident light was focused on the samples using a microscope objective and the transmitted light was collected by a collective lens for delivering to a spectrometer (Ocean Optics QE-pro).

To investigate the in-plane scattering of such arrays, we utilized the setup schematically shown in Fig. 1(b). In this setup a broad white light was focused on the samples with a microscope objective with 0.5 numerical aperture (objective 1). The in-plane scattering was collected by another micro-

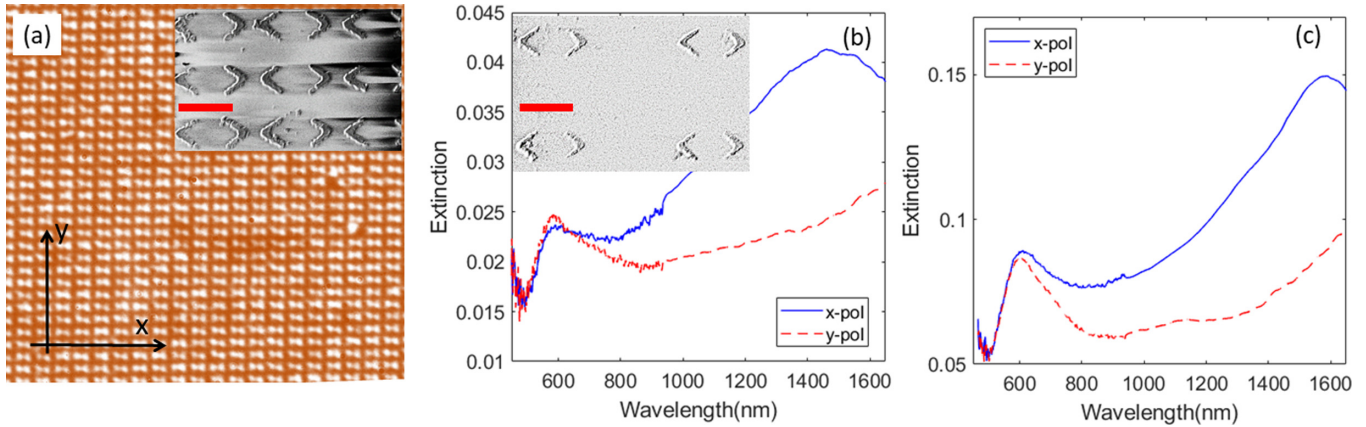


FIG. 6. (a) Optical and scanning electron microscope (SEM) images (inset) of sample 1. Also shown are the extinction spectra of (b) sample 2 and (c) sample 1 (c) for x polarization (solid line) and y polarization (dashed line). The inset in (b) shows the SEM image of sample 2. The scale bars in the insets of (a) and (b) are $1\ \mu\text{m}$.

scope objective with numerical aperture of 0.85 (objective 2). This objective was on a translation stage, allowing it to move horizontally along the edges of the samples. The scattered light was detected along the x and y axes, highlighting how such a process is influenced by the angle of views and sides of the V-shaped nanoantennas. Figures 7(a) and 7(b) show the geometrical positions of objective 2 along the substrates of samples 1 and 2. For measuring the in-plane scattering along the x axis, this objective moves along the y axis from 0 to 20 mm, i.e., the whole length of the substrate [Fig. 7(a)]. For the case of the in-plane scattering along the y axis, objective 2 moves along the x axis over a similar range of 0–20 mm [Fig. 7(b)]. For each of these cases, the incident polarization axis was adjusted to be along certain directions. As highlighted in Fig. 7, these were $\theta = -45^\circ$ (red double-sided arrows), $\theta = 0^\circ$ (x axis), $\theta = 45^\circ$ (blue double-sided arrows), and $\theta = 90^\circ$ (y axis).

IV. EXPERIMENTAL VERIFICATION OF THE SUPERCELLS

The extinction spectra of samples 1 and 2 can provide key information regarding their mode properties and formation of the supercells discussed in the preceding section. Such

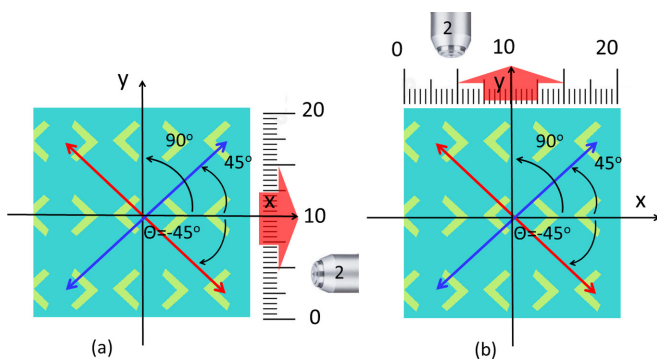


FIG. 7. Experimental configurations for the measurements of in-plane scattering along the (a) x axis and (b) y axis. The double-sided arrows show the directions of the incident light polarization. The θ are the angles between these directions and the x axis.

spectra are shown in Figs. 6(b) and 6(c) for the cases when the incident light was polarized along the x axis (solid lines) and the y axis (dashed lines), i.e., for x polarization and y polarization, respectively. For x polarization the results for sample 1 suggest the formation of a peak at 611 nm and another peak at 1580 nm [Fig. 6(c)]. For y polarization a small peak happens at about 600 nm, but the long-wavelength peak goes beyond the sensitivity range of our spectrometers (dashed line). These are consistent with the numerical results shown in Fig. 1(c). In particular, the peak at 1580 in Fig. 6(c) matches well the 1490 peak in Fig. 1(c), indicating the formation of the $> + <$ supercells.

The extinction spectra of sample 2 suggest a peak at about 600 nm for both x polarization and y polarization [Fig. 6(b)]. For x polarization the longer-wavelength peak of this sample occurs at about 1477 nm and seems to be broader than that of sample 1. These results suggest a blueshift of about 100 nm, compared to that of sample 1. This can be associated with the fact that in the case of sample 2 the coupling between V-shaped nanoantennas of the neighboring cells is much weaker. Therefore, although the quadrupole modes associated with the x polarization happens, the lack of intercell coupling prevent the formation of $> + <$ supercells. Similar to the case of sample 1, experimentally we could not detect the peak associated with the $< + >$ supercells of this sample, as its wavelength was beyond our detector's sensitivity range. Note also that, for the cases of both samples, the jaggedness and nonuniformity of the V-shaped nanoantennas led to significant broadening of the spectra.

V. IN-PLANE SCATTERING AND POLARIZATION CONTROL

The results for the measurements of the in-plane scattering for sample 1 along the x axis when $\theta = -45^\circ$, 0° , 45° , and 90° are shown in Figs. 8(a)–8(d), respectively. For all polarization cases, we can see scattering in wide wavelength ranges from about 600 to 1050 nm. These results are limited by the sensitivity range of our spectrometer, but the sharp cuts at 1050 nm suggest the possibility of extension of such scattering farther into the infrared range. A feature seen in Fig. 8(d) is

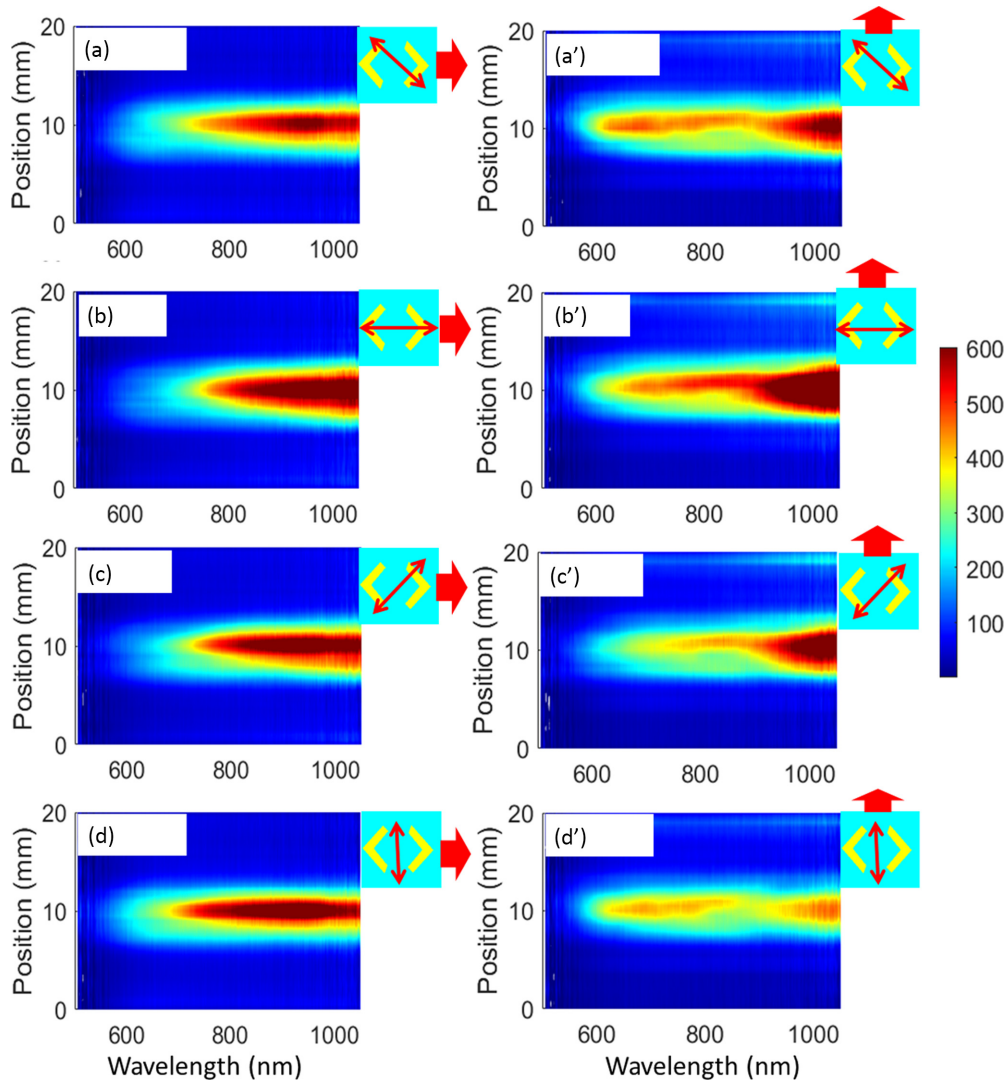


FIG. 8. In-plane scattering of sample 1 along the (a)–(d) x axis and (a')–(d') y axis as a function of position (see Fig. 7) for (a) and (a') $\theta = -45^\circ$, (b) and (b') $\theta = 0^\circ$, (c) and (c') $\theta = 45^\circ$, and (d) and (d') $\theta = 90^\circ$. The color-coded bar shows the amount of in-plane scattering counts.

that for $\theta = 90^\circ$ (y polarization) the extension of the scattered light into the visible range is more prominent than the case of $\theta = 0^\circ$ [Fig. 8(b)]. Note that in these figures the vertical axes refer to the positions of objective 2 along the edges of the glass substrate, i.e., the y axis [Fig. 7(a)].

The situation changes significantly when the scattering is detected along the y axis [Fig. 7(b)]. As shown in Fig. 8(b ii), in this case when the incident light is polarized along the x axis ($\theta = 0^\circ$), we have a relatively high scattering intensity in the near-infrared range. In the visible range, however, compared to the case seen in Fig. 8(b i), here the in-plane scattering is emerging from the edge of the substrate in a more inhomogeneous way while it is spectrally broader. In other words, within the 900–1050 nm range the spatial extent of the scattering is about 4 mm, while for a wavelength range of 600–900 nm it is mostly localized in about 2 mm. This suggests significant spectral variations of the scattered light as a function of the location of objective 2 [Fig. 7(b)].

When the polarization of the incident light is along the y axis, i.e., $\theta = 90^\circ$ [Fig. 8(d ii)], the amount of scattering

is reduced. Under this condition, the scattering spectrum is uniquely maximized in two separate wavelength ranges, i.e., visible and near-infrared ranges [Fig. 8(d ii)]. The results in Fig. 8 also show that, when the scattering is detected along the y axis, for $\theta = -45^\circ$ [Fig. 8(a ii)] and 45° [Fig. 8(c ii)] one can see a significant contrast with those when the in-plane scattering was detected along the x axis [Figs. 8(a i) and 8(c i)]. These include spectrally wider ranges and more pronounced position-dependent in-plane scattering. The combination of these results suggests a multidirectional in-plane scattering process in sample 1. For the case of Figs. 8(a ii)–8(d ii), in particular, we can see clearly the asymmetry impact of $\theta = -45^\circ$ and 45° when viewed along the y axis. The results for sample 2 follow similar patterns but with much less intensity.

To further study the in-plane scattering properties of the $\langle \rangle$ arrays, we analyze its polarization by placing an analyzer before the spectrometer [Figs. 9(a) and 9(b)]. Here ϕ refers to angle of the analyzer axis from the normal of the sample plane. Figure 9(c) shows the results when the analyzer axis was horizontal, i.e., $\phi = 90^\circ$, and the light was collected along

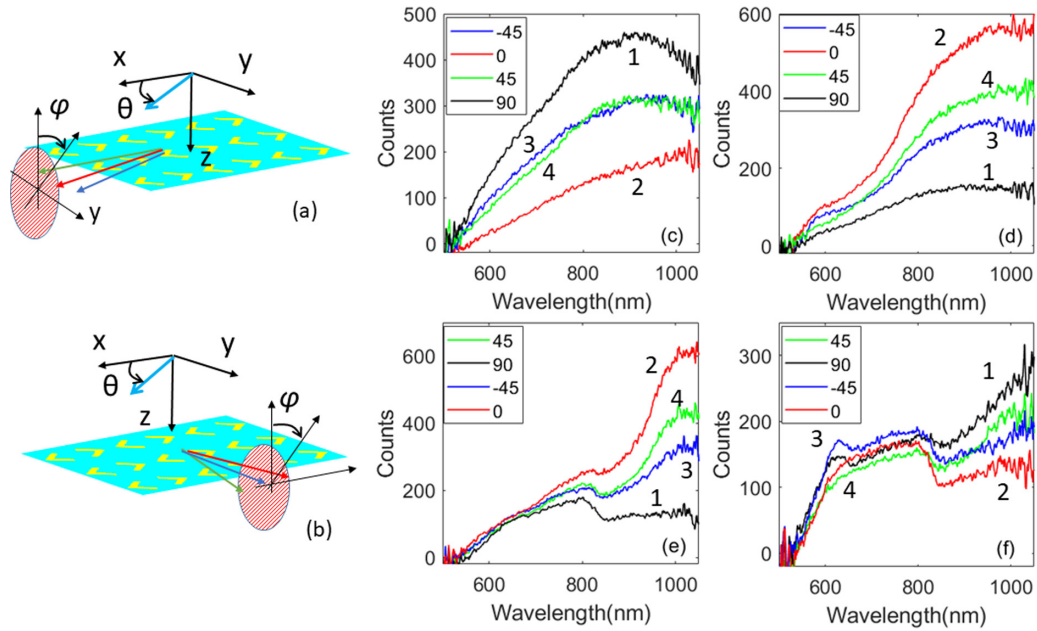


FIG. 9. Experimental configurations for in-plane scattering measurement along the (a) x and (b) y axes. In 9(c)–9(f) lines 1–4 refer to the cases when $\theta = 90^\circ, 0^\circ, -45^\circ$, and 0° , respectively. In (c) and (d) detection is along the x axis and $\phi = 90^\circ$ and 0° , respectively. In (e) and (f) detection is along the y axis and $\phi = 90^\circ$ and 0° , respectively.

the x axis [Fig. 9(a)]. These results show that variations of the θ leads to significant changes in the scattered light. For $\theta = 90^\circ$ the maximum light is detected with a characteristic broad peak at about 925 nm (line 1). For $\theta = 0^\circ$ the amount of scattered light decreases and the peak disappears (line 2). For these cases the in-plane scattering intensities remain comparable, indicating a mix of polarization states. This can be seen further if we consider the cases of $\theta = -45^\circ$ (line 3) and $\theta = 45^\circ$ (line 4). The similarity of these results can be related to the symmetry of the $\langle \rangle$ arrays when in-plane scattering is detected along the x axis.

When the light is detected along the x axis and the polarization axis of the analyzer is rotated by 90° , i.e., $\phi = 0^\circ$, the results suggest that the maximum scattering occurs when $\theta = 0^\circ$ [Fig. 9(d), line 2]. For $\theta = 90^\circ$ the amount of light is reduced, but no significant spectral changes can be seen [Fig. 9(d), line 1]. The results for $\theta = -45^\circ$ and 45° (lines 3 and 4) also show similar features. The combination of these results suggests that the $\langle \rangle$ array supports elliptical scattering polarization controlled by the linearly polarized incident light.

The results when the scattered light is collected along the y axis are shown in Figs. 9(e) and 9(f). When the incident light is polarized along the x axis ($\theta = 0^\circ$) and $\phi = 90^\circ$, the spectrum of the scattered light contains two peaks. These include a small peak at about 800 nm and a major one at about 1000 nm [Fig. 9(e), line 2]. When the incident light polarization is rotated by 90° ($\theta = 90^\circ$), the longer-wavelength peak mostly disappears, while the shorter-wavelength peak still remains resolvable [Fig. 9(e), line 1]. These results suggest that, because of the shape of the nanoantennas, the spectra of the in-plane scattering for different states of polarization are different.

For the case when the scattered light is detected along the y axis and $\phi = 0^\circ$, a prominent feature occurs around

the 600–800 nm range [Fig. 9(f)]. This figure shows that the amount of scattered light for $\theta = -45^\circ$ (line 3) is more than those when $\theta = 0^\circ$ (line 2), 45° (line 4), and 90° (line 1). This can be associated with the fact that for the cases of $\theta = -45^\circ$ and 45° , the light polarization is approximately along one of the arms of the V-shaped nanoantennas [Figs. 3(e) and 3(f)]. In each of these cases one arm supports the high-order longitudinal mode while the other arm supports the transverse mode with lower order. This makes the charge configuration and plasmon oscillations, as viewed along the y axis, asymmetric for the cases of $\theta = -45^\circ$ and 45° . The phase relations associated with such configuration may be responsible for the higher scattering in the 600–800 nm range for the case of $\theta = -45^\circ$ [Fig. 9(f), line 3]. This further highlights the unique polarization states of the in-plane scattering of $\langle \rangle$ nanoantennas arrays and their control via the incident light polarization.

Note that the term plasmonic conjugate used in this paper is primarily associated with the geometrical coupling of $> + <$, against that of $< + >$. In fact, these two supercells, which support two different types of near-field couplings, hybridization processes, and charge configurations [Figs. 3(b) and 3(d)], are associated with the inward and outward couplings of a pair of the V-shaped nanoantennas. These features and the distinct well-resolved spectral features of such supercells can provide wider control over the functionalities of plasmonic metasurfaces and their device applications. This may include active optical filters in the infrared range. Additionally, the results in Fig. 2(b) suggest coherent coupling between the multipolar hybridized modes of many $> + <$ supercells. Considering this feature, the optical switching between $< + >$ and $> + <$ may offer a unique way to actively control hybridization of multipolar modes associated with these cells.

VI. CONCLUSION

We studied optical properties of metasurfaces consisting of periodic arrays of Au V-shaped nanoantennas. We showed such arrays can support two supercells and their polarization optical switching. In one of the supercells, i.e., $\langle + \rangle$, the nanoantennas of a given unit cell of the array are coupled face to face. We showed that such supercells tend to be isolated. In another type of supercell the V-shaped nanoantennas of the adjacent unit cells are coupled to each other, forming a plasmonic conjugate system ($\rangle + \langle$). We showed that such supercells can couple to the lattice modes of the arrays, extending coherent information across the arrays along one dimension. We showed that the optical features associated

with $\langle + \rangle$ and $\rangle + \langle$ include two strong infrared extinction peaks spectrally located at two distant wavelengths. Our results for the in-plane scattering of such metasurfaces offer strong polarization mixing which can be controlled using the incident light polarization. This indicates that asymmetry of optical excitation of the V-shaped nanoantennas, as viewed from the side, can be a crucial asset to coherently control their in-plane scattering.

ACKNOWLEDGMENT

This work was supported by the U.S. National Science Foundation under Grant No. NSF-ECCS-1917544.

-
- [1] F. Aieta, P. Genevet, M. A. Kats, N. Yu, R. Blanchard, Z. Gaburro, and F. Capasso, *Nano Lett.* **12**, 4932 (2012).
 - [2] N. Yu, F. Aieta, P. Genevet, M. A. Kats, Z. Gaburro, and F. Capasso, *Nano Lett.* **12**, 6328 (2012).
 - [3] N. Meinzer, W. L. Barnes, and I. R. Hooper, *Nat. Photon.* **8**, 889 (2014).
 - [4] A. V. Kildishev, A. Boltasseva, and V. M. Shalaev, *Science* **339**, 1232009 (2013).
 - [5] A. S. Solntsev, G. S. Agarwal, and Y. S. Kivshar, *Nat. Photon.* **15**, 327 (2021).
 - [6] P. Georgi, M. Massaro, K.-H. Luo, B. Sain, N. Montaut, H. Herrmann, T. Weiss, G. Li, C. Silberhorn, and T. Zentgraf, *Light Sci. Appl.* **8**, 70 (2019).
 - [7] H.-T. Chen, A. J. Taylor, and N. Yu, *Rep. Prog. Phys.* **79**, 076401 (2016).
 - [8] M. A. Kats, P. Genevet, G. Aoust, N. Yu, R. Blanchard, F. Aieta, Z. Gaburro, and F. Capasso, *Proc. Natl. Acad. Sci. USA* **109**, 12364 (2012).
 - [9] L. Liu, X. Zhang, M. Kenney, X. Su, N. Xu, C. Ouyang, Y. Shi, J. Han, W. Zhang, and S. Zhang, *Adv. Mater.* **26**, 5031 (2014).
 - [10] J. Wang and J. Du, *Appl. Sci.* **6**, 239 (2016).
 - [11] J. Hu, S. Bandyopadhyay, Y.-h. Liu, and L.-y. Shao, *Front. Phys.* **8**, 586087 (2021).
 - [12] V. G. Kravets, A. V. Kabashin, W. L. Barnes, and A. N. Grigorenko, *Chem. Rev.* **118**, 5912 (2018).
 - [13] R. R. Gutha, S. M. Sadeghi, C. Sharp, and W. J. Wing, *Nanotechnology* **28**, 355504 (2017).
 - [14] X. Zhang, S. Feng, J. Zhang, T. Zhai, H. Liu, and Z. Pang, *Sensors* **12**, 12082 (2012).
 - [15] B. D. Thackray, V. G. Kravets, F. Schedin, G. Auton, P. A. Thomas, and A. N. Grigorenko, *ACS Photon.* **1**, 1116 (2014).
 - [16] Y. Sonnefraud, N. Verellen, H. Sobhani, G. A. Vandenbosch, V. V. Moshchalkov, P. Van Dorpe, P. Nordlander, and S. A. Maier, *ACS Nano* **4**, 1664 (2010).
 - [17] J. Li, J. Ye, C. Chen, L. Hermans, N. Verellen, J. Ryken, H. Jans, W. Van Roy, V. V. Moshchalkov, L. Lagae, and P. Van Dorpe, *Adv. Opt. Mater.* **3**, 176 (2015).
 - [18] S. M. Sadeghi, W. J. Wing, and Q. Campbell, *J. Appl. Phys.* **119**, 244503 (2016).
 - [19] S. M. Sadeghi, R. R. Gutha, and W. J. Wing, *Opt. Lett.* **41**, 3367 (2016).
 - [20] R. R. Gutha, S. M. Sadeghi, A. Hatef, C. Sharp, and Y. Lin, *Appl. Phys. Lett.* **112**, 223102 (2018).
 - [21] M. Ramezani, G. Lozano, M. A. Verschuuren, and J. Gómez-Rivas, *Phys. Rev. B* **94**, 125406 (2016).
 - [22] D. Wang, A. Yang, W. Wang, Y. Hua, R. D. Schaller, G. C. Schatz, and T. W. Odom, *Nat. Nanotechnol.* **12**, 889 (2017).
 - [23] A. Yang, Z. Li, M. P. Knudson, A. J. Hryn, W. Wang, K. Aydin, and T. W. Odom, *ACS Nano* **9**, 11582 (2015).
 - [24] S. M. Sadeghi, W. Wing, R. R. Gutha, C. Sharp, D. Roberts, and C. Mao, *J. Mater. Chem. C* **9**, 14269 (2021).
 - [25] S. M. Sadeghi, R. R. Gutha, and C. Sharp, *J. Mater. Chem. C* **7**, 9678 (2019).
 - [26] S. M. Sadeghi and R. R. Gutha, *Phys. Rev. Appl.* **15**, 034018 (2021).
 - [27] S. M. Sadeghi and R. R. Gutha, *Appl. Mater. Today* **22**, 100932 (2021).
 - [28] D. Vercrucy, Y. Sonnefraud, N. Verellen, F. B. Fuchs, G. Di Martino, L. Lagae, V. V. Moshchalkov, S. A. Maier, and P. Van Dorpe, *Nano Lett.* **13**, 3843 (2013).
 - [29] D. Vercrucy, X. Zheng, Y. Sonnefraud, N. Verellen, G. Di Martino, L. Lagae, G. A. Vandenbosch, V. V. Moshchalkov, S. A. Maier, and P. Van Dorpe, *ACS Nano* **8**, 8232 (2014).
 - [30] Y. Yu, J. Liu, Y. Yu, D. Qiao, Y. Li, and R. Salas-Montiel, *Opt. Express* **30**, 7918 (2022).
 - [31] J. Li, N. Verellen, D. Vercrucy, T. Bearda, L. Lagae, and P. Van Dorpe, *Nano Lett.* **16**, 4396 (2016).
 - [32] J. Guan, M. R. Bourgeois, R. Li, J. Hu, R. D. Schaller, G. C. Schatz, and T. W. Odom, *ACS Nano* **15**, 5567 (2021).
 - [33] G. Lu, Y. Wang, R. Y. Chou, H. Shen, Y. He, Y. Cheng, and Q. Gong, *Laser Photon. Rev.* **9**, 530 (2015).
 - [34] Y. Y. Tanaka and T. Shimura, *Nano Lett.* **17**, 3165 (2017).
 - [35] B. Auguie, X. M. Bendana, W. L. Barnes, and F. J. García de Abajo, *Phys. Rev. B* **82**, 155447 (2010).
 - [36] N. Mahi, G. Lévêque, O. Saison, J. Marae-Djouda, R. Caputo, A. Gontier, T. Maurer, P.-M. Adam, B. Bouhaf, and A. Akjouj, *J. Phys. Chem. C* **121**, 2388 (2017).
 - [37] V. Kravets, F. Schedin, and A. Grigorenko, *Nat. Commun.* **3**, 640 (2012).
 - [38] A. D. Utyushev, V. I. Zakomirnyi, and I. L. Rasskazov, *Rev. Phys.* **6**, 100051 (2021).
 - [39] L. Lin and Y. Yi, *Opt. Express* **23**, 130 (2015).